Published online 5 June 2019

Nucleic Acids Research, 2019, Vol. 47, No. 13 ***6885–6899***
doi: 10.1093/nar/gkz494

A Mn-sensing riboswitch activates expression of a Mn^{2+}/Ca^{2+} ATPase transporter in Streptococcus

Julia E. Martin[1,*,†], My T. Le[2,†], Nabin Bhattarai[1], Daiana A. Capdevila[3], Jiangchuan Shen[4], Malcolm E. Winkler[5] and David P. Giedroc[3]

[1]Department of Biological Sciences, Idaho State University, Pocatello, ID 83209, USA, [2]Department of Cell Biology, Faculty of Biological Sciences, Vietnam National University, Hanoi, Vietnam, [3]Department of Chemistry, Indiana University, Bloomington, IN 47405, USA, [4]Department of Cellular and Molecular Biochemistry, Indiana University, Bloomington, IN 47405, USA and [5]Department of Biology, Indiana University, Bloomington, IN 47405, USA

Received March 21, 2019; Revised May 08, 2019; Editorial Decision May 14, 2019; Accepted May 31, 2019

ABSTRACT

Maintaining manganese (Mn) homeostasis is important for the virulence of numerous bacteria. In the human respiratory pathogen *Streptococcus pneumoniae*, the Mn-specific importer PsaBCA, exporter MntE, and transcriptional regulator PsaR establish Mn homeostasis. In other bacteria, Mn homeostasis is controlled by *yybP-ykoY* family riboswitches. Here, we characterize a *yybP-ykoY* family riboswitch upstream of the *mgtA* gene encoding a P_{II}-type ATPase in *S. pneumoniae,* suggested previously to function in Ca^{2+} efflux. We show that the *mgtA* riboswitch aptamer domain adopts a canonical *yybP-ykoY* structure containing a three-way junction that is compacted in the presence of Ca^{2+} or Mn^{2+} at a physiological Mg^{2+} concentration. Although Ca^{2+} binds to the RNA aptamer with higher affinity than Mn^{2+}, *in vitro* activation of transcription read-through of *mgtA* by Mn^{2+} is much greater than by Ca^{2+}. Consistent with this result, *mgtA* mRNA and protein levels increase ≈5-fold during cellular Mn stress, but only in genetic backgrounds of *S. pneumoniae* and *Bacillus subtilis* that exhibit Mn^{2+} sensitivity, revealing that this riboswitch functions as a failsafe 'on' signal to prevent Mn^{2+} toxicity in the presence of high cellular Mn^{2+}. In addition, our results suggest that the *S. pneumoniae yybP-ykoY* riboswitch functions to regulate Ca^{2+} efflux under these conditions.

INTRODUCTION

Small non-coding regulatory RNAs (sRNAs) are ubiquitous and found in all domains of life and play myriad roles in regulating gene expression (1,2). In bacteria, these sRNAs exist as short transcripts with lengths of 30–500 nucleotides (3,4). Bacterial sRNAs are broadly classified into two categories: *cis*-acting (riboswitches) or *trans*-acting (independent transcripts) RNAs. *Trans*-acting sRNAs modulate the stability or translation of mRNA transcript(s) by imperfect base-pairing interactions (5,6) at or near the ribosome binding site (RBS) on the target transcript. Riboswitches, on the other hand, are highly structured regulatory segments located within the 5′ untranslated regions (UTRs) of mRNAs that interact with small molecules, such as metals and other ligands, resulting in a change in transcription or translation mediated directly by environmental changes. sRNAs may also interact with RNA-binding proteins thereby modifying their activities (7,8).

Bacterial sRNAs function in many cellular processes, including the response to environmental stresses, e.g. those mediated by the immune system, and maintaining homeostasis (5,9). Accumulating evidence suggests that sRNAs are differentially expressed in bacteria when transitioning from colonization to an active infection which suggests that sRNAs are key players in mediating invasive disease (10–13). *Streptococcus pneumoniae* is a Gram-positive bacterium that commonly colonizes the nasopharynx of healthy individuals, persisting as a harmless bacterial commensal (14). Despite a largely asymptomatic colonization, *S. pneumoniae* remains a leading causative agent of sinusitis, otitis media (middle ear infection), and the life-threatening invasive diseases pneumonia, bacteremia, and meningitis globally (15,16). Transition from the harmless commensal to pathogen often occurs after a viral respiratory tract infection and is triggered by numerous factors, many of which are unknown (14). Progression into the lungs and intrusion into the circulatory system, exposes the pneumococcus to numerous stress conditions and environmental

*To whom correspondence should be addressed. Tel: +1 208 282 1277; Fax: +1 208 282 4570; Email: martjul8@isu.edu
†The authors wish it to be known that, in their opinion, the first two authors should be regarded as Joint First Authors.

changes (17), including transition metal fluctuations, an important mediator in the 'fight or flight' response during infection (18,19). The capacity for bacteria to quickly adapt to these different environments may derive in part from sRNAs modulating the expression of virulence factors.

Multiple (>100) sRNAs have been identified in *S. pneumoniae* (20–25), but the functional role for most of these remains unknown. One particular candidate sRNA, SN44, identified in *S. pneumoniae* TIGR4 using genome-tilling arrays (21) is of interest here. SN44 is predicted on the basis of sequence homology to be a *cis*-acting *yybP-ykoY* family response element (riboswitch) that is conserved among different *Streptococcus* species (21) (Supplementary Figure S1). The *yybP-ykoY* motif defines a ubiquitous class of riboswitches that are upstream of genes that encode uncharacterized or poorly characterized proteins many of which have been linked to Mn^{2+} homeostasis. To date, *yybP-ykoY*-regulated gene products, MntP of *Escherichia coli* (26), MntX of *Neisseria* spp. (27), and YaoB (a predicted P-type II ATPase) of *Lactococcus lactis* (28), have been independently implicated as Mn^{2+} efflux transporters capable of relieving cellular Mn toxicity. Other studies show that several of these associated *yybP-ykoY* family riboswitches respond to high Mn^{2+} *in vitro* and *in vivo* modulating transcription and translation of downstream gene(s) within the transcript (28–30). Although *yybP-ykoY* riboswitches have generally been observed to bind Mn^{2+} *in vitro* with highest affinity among other transition metals examined, none thus far exhibit strict Mn^{2+} specificity (30).

The *yybP-ykoY* riboswitch aptamer domain adopts a four-helix junction architecture with P2 stacked on P1 and P4 stacked on P3, with the transition metal sensing pocket formed by nucleotides in the L1 loop (in P1) and L3 loop in P3 (Figure 1A). P2 and P4 are not strictly conserved and can be replaced by a short single-stranded connecting region or a longer helical stem, just above the cross-over point (Figure 1). A recent structural analysis of the *L. lactis yybP-ykoY* riboswitch aptamer domain suggests that the metal site may well be plastic and capable of adopting a range of coordination structures and nuclearity, with binuclear and trinuclear metal (Cd^{2+}) complexes observed in that study (30). The binuclear site in a previous structure of the *L. lactis yaoB* riboswitch (28) was modeled as Mg^{2+} or Mn^{2+} in the M_A site and Mn^{2+} in the M_B site (Figure 2A). The M_B site is thought to provide specificity for Mn^{2+} given the presence of five inner-sphere coordination bonds, including the N7 of A41 in the L3 loop (Figure 2A–C).

Like other annotated *yybP-ykoY* family riboswitches, the putative SN44 riboswitch overlaps the RBS within the target gene transcript and features a transcription terminator helix just 5′ to the RBS (Supplementary Figure S1). The SN44 RNA in *S. pneumoniae* D39 serotype 2 is encoded within the 5′ UTR of the *mgtA* (*spd_1383*; previously *caxP* or PacL) transcript, encoding a P_{II}-type ATPase transporter. MgtA was previously suggested to function in Ca^{2+} efflux (25,31), while in a different report was suggested to be implicated in the response against Zn^{2+} and Mn^{2+} toxicity also (32). The idea that MgtA in *S. pneumoniae* is not restricted to Ca^{2+} and could also transport Mn^{2+} is also supported by the fact that the MgtA protein is encoded from the negative-sense DNA strand immediately upstream of the *mntE* gene, which encodes the constitutively expressed Mn^{2+}-specific cation diffusion facilitator exporter MntE (33,34). Both MgtA and MntE are important for the virulence of *S. pneumoniae* (31,33). Despite intensive study, the physiological roles of many genes critical for virulence, including those encoding divalent metal transporters like MgtA, remain unclear.

In this study, we examine the metal binding and metal-induced folding of the *mgtA* aptamer and the regulation of *mgtA* in *S. pneumoniae* D39 strain. We find that the *S. pneumoniae* D39 *mgtA* aptamer RNA binds stoichiometric Mn^{2+} and Ca^{2+} in a background of physiological Mg^{2+} and each is capable of stabilizing the same compact conformation; however, Mn^{2+} stimulates *in vitro* read-through transcription to a far greater extent than Ca^{2+}. We establish for the first time that the *mgtA* mRNA is upregulated during Mn-stress in this organism, and that this increased transcription *in vivo* requires the *mgtA* (*yybP-ykoY* family) riboswitch. Further investigation reveals that MgtA may export Mn^{2+} under conditions of extreme Mn-stress thereby protecting cells from Mn^{2+} toxicity. The *mgtA* riboswitch may also function to regulate Ca^{2+} export under these conditions.

MATERIALS AND METHODS

See Supplementary Material detailing methods for bacterial strain and plasmid construction, bacterial growth, disk diffusion assay, β-galactosidase activity assay, RNA isolation and quantitative real-time PCR, western blot, *yybP-ykoY* RNA synthesis, and inductively coupled plasma-mass spectrometry (ICP-MS) for measurement of total cell-associated divalent cationic metals. Bacterial strains and plasmids used in this study are listed in Supplementary Table S1 and relevant DNA oligonucleotide primers in Supplementary Tables S2 and S3.

Native polyacrylamide gel electrophoresis (PAGE) analysis of *yybP-ykoY* RNAs (35)

Purified RNA (2 μg) was heated at 90°C for 2 min followed by incubation at room temperature for 3 min, then subsequently allowed to refold in 50 mM HEPES [pH 7.5], 50 mM NaCl at room temperature for 10 min. Various divalent metal ion concentrations ranging from 0.01 to 5 mM were added and RNA mixture was left at room temperature for an additional 30 min prior to mixing with loading dye (10% glycerol and 0.01% xylene cyanol). RNA was separated by native PAGE (8% gel prepared with 19:1 acrylamide/bisacrylamide) at 4°C in running buffer containing 34 mM Tris, 66 mM HEPES [pH 7.5], and 3 mM $MgCl_2$, which was recirculated every hour. RNA was stained with ethidium bromide and observed with a Gbox (Biorad).

SHAPE probing

SHAPE was performed as previously described using 1-methyl-7-nitroisatoic anhydride (1M7) derivatization

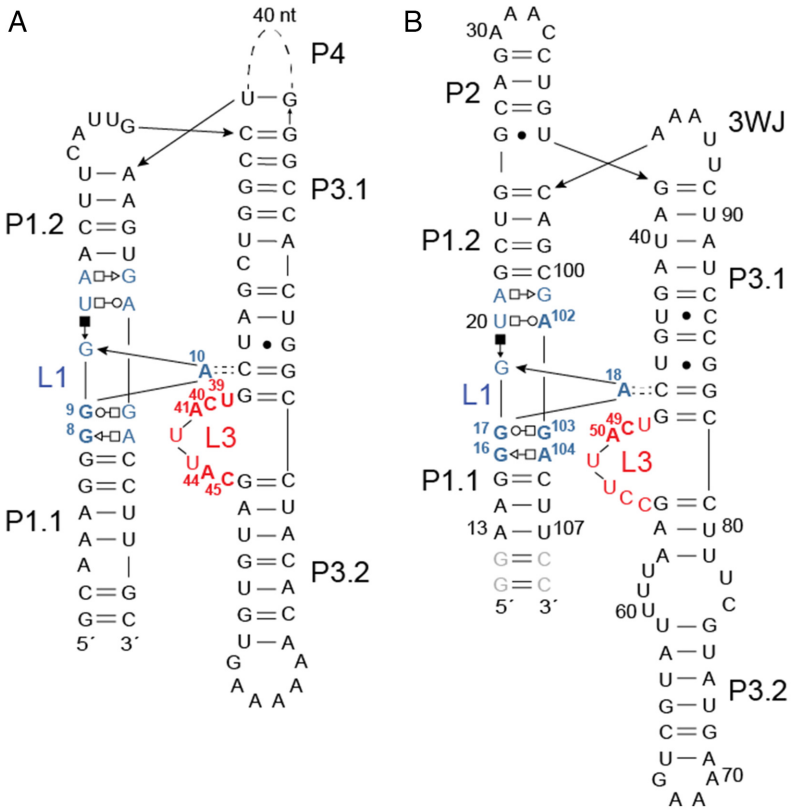

Figure 1. Secondary structure diagrams of the aptamer domains of (**A**) *E. coli alx* sequence (30) and (**B**) *Streptococcus pneumoniae* D39 *mgtA* riboswitch domains. In panel A, nucleotides in L1 (*blue*) and in L3 (*red*) that correspond to those shown in the structural models (Figure 2) are highlighted in *bold*, and correspond to the numbering convention of the *L. lactis yybP-ykoY* riboswitch (see Figure 2A) (28). In panel B, we used the natural nucleotide residue numbers, and those nucleotides targeted for substitution in this work in L1 (*blue*) and L3 (*red*) are highlighted in bold. For example, the loop L1 G8-G9-A10 *L. lactis* system corresponds to the G16-G17-A18 in the *S. pneumoniae* RNA, while the *L. lactis* C40-A41 L3 sequence corresponds to the C49-A50 sequence in *S. pneumoniae*. A41 in the *L. lactis* RNA (A50 in the *mgtA* RNA) makes an inner sphere coordination bond with the MnB metal (see Figure 2A). The *gray* nucleotides in panel B are non-native and were added for *in vitro* transcription.

reagent (36–38). RNA constructs consisted of the wild-type sequence from the *S. pneumoniae* D39 *mgtA* 5′ UTR (containing the *yybp-ykoY* aptamer domain) flanked by SHAPE flanking sequences (37). RNAs were *in vitro* transcribed from PCR templates and purified similarly to that described above for RNA synthesis. Purified RNAs (10 pmol) was refolded in 50 mM HEPES, pH 7.5, 50 mM NaCl buffer before 1M7 derivatization. Reverse transcription of the derivatized RNA was performed with a FAM 6-labeled reverse primer. Unmodified RNA (2 pmol) used as a sequencing ladder was synthesized using reverse transcriptase, NED-labeled reverser primer, and ddCTP or ddGTP. An equal volume of sequencing ladder and reaction mixture with and without 1M7 was precipitated with 0.3 M sodium acetate, pH 5.2 and 100% ethanol, washed with 70% ethanol, air-dried, and re-dissolved in 15 μl water. Fragment analysis was performed using capillary electrophoresis by GENEWIZ (Plainfield, NJ, USA). Data processing was performed using QuShape following a protocol as previously described (39).

Small angle X-ray scattering (SAXS)

Small angle and wide angle X-ray scattering data were acquired at three different RNA concentrations (0.8, 1.6 and 3.2 mg/ml) of select RNAs folded in buffer containing 50 mM HEPES, pH 7.5, 50 mM NaCl, 3 mM $MgCl_2$ and 0.5 mM of the metal ion indicated. Data were collected at beam line 12-ID of the Advanced Photon Source at the Argonne National Laboratory. The wavelength (λ) of X-ray radiation was set to 1.033 Å. Procedures for SAXS/WAXS measurement were similar to those previously described (40,41). Thirty images were collected for each RNA concentration and its corresponding background buffer.

SAXS data were averaged, and the background was subtracted using the NCI-SAXS program package. The averaged scattering profiles of three RNA concentrations were merged using PRIMUS in the ATSAS program package (http://www.embl-hamburg.de/biosaxs/). A GUINIER plot was generated as $\ln(I(q))$ versus q^2 to check sample quality and to obtain I_0 and the radius of gyration (R_g) within the range of $q_{max}*R_g < 1.3$. The data from each RNA concentration were normalized with I_0. Conformation of the RNAs was examined using the Kratky plot for $q < 0.3$ Å^{-1}. Scattering profiles of RNAs were then Fourier-transformed using GNOM of the ATSAS package to obtain the normalized pair distance distribution graph.

Ab in initio modeling was performed using the program DAMMIN in a slow mode (42). For each RNA, 10 models

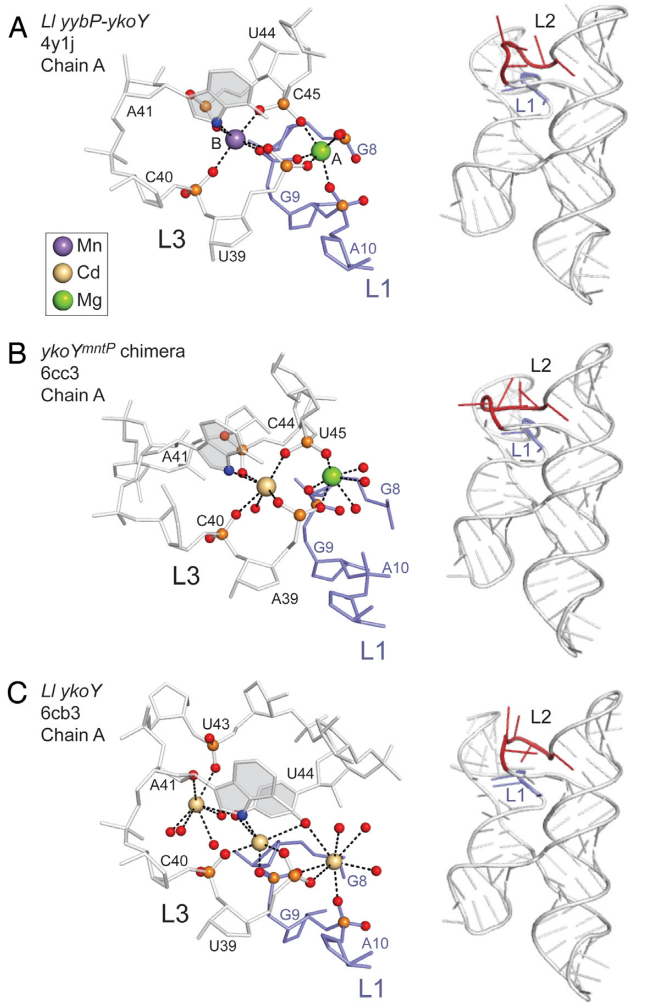

Figure 2. Regulatory metal coordination site region (*left*) and global ribbon diagrams (*right*) of the various *yybP-ykoY* riboswitch aptamer domains. (**A**) *L. lactis yybP-ykoY* riboswitch bound to Mg^{2+} (site A) and the Mn^{2+} (site B) (28); (**B**) chimeric *E. coli ykoY*^{mntP} riboswitch bound to Mg^{2+} (site A) and Cd^{2+} (site B) (30) and (**C**) the three metal (Cd^{2+})-bound form of the *L. lactis yaoB* riboswitch (30).The nucleotide numbering convention in panels B and C are as adopted for the *L. lactis yybP-ykoY* riboswitch (panel A). L1 residues are highlighted in blue, and L3 residues are shown in gray (*left*) or red (*right*) of panels A-C. The nucleotide base of L3 nucleotide A41 is shaded *gray* since N7 donates a coordination bond to the Mn^{2+} (A) and Cd^{2+} (B, C) ions in these structures.

were obtained, filtered, and averaged using the DAMPUP, DAMFILT and DAMAVER of the ATSAS package (http://www.embl-hamburg.de/bioSAXS). Normalized spatial discrepancy (NSD) between each pair of the models was computed. The model with the lowest NSD value was selected as the reference model for superimposing onto other models. Outliner models (two models) with an NSD above mean +2* variation were removed before averaging.

Isothermal titration calorimetry

ITC experiments were performed following standard protocol previously described (30). Briefly, RNAs were heated at 95°C for 2 min, cooled down at room temperature for 3 min, diluted into ITC buffer (30 mM HEPES [pH 6.8], 150 mM NaCl), and incubated at room temperature for an additional 10 min. $MgCl_2$ was then added to a final concentration of 3 mM and the RNA was subsequently incubated at room temperature for 30 min. RNAs were dialyzed into ITC buffer containing 3 mM $MgCl_2$, filtered using a 3 kDa MWCO column, and degassed prior to ITC measurement. Divalent metal cations were dissolved in ITC buffer, filtered, and degassed. Experiments were performed with 50–100 μM RNA and 0.5 to 2 mM metal cation at 25°C, depending on affinity and magnitude of enthalpy. Divalent metal cation was injected with 0.5 to 1 ul volume every 300 s. Data were corrected for heats of dilution by subtracting the enthalpies of cations titrated into the ITC buffer from raw data and analyzed using an independent binding model by Nanoanlyze (TA instrument).

IVT termination assay

In vitro transcription termination assays were performed using standard protocols (28,43). To construct the *in vitro* transcription plasmid, the *S. pneumoniae mgtA* 5′-UTR (containing the aptamer domain, intrinsic terminator, and the first 45-nt of the MgtA protein coding sequence) was fused to a *B. subtilis glyQS* promoter. An ApC dinucleotide sequence was added to the 5′ end of the *mgtA* aptamer domain with no cytosines present in the next 12 nucleotides. DNA templates were produced by PCR and spin column purified (Qiagen). To assemble stalled RNA polymerase complexes, 20 mM template was mixed with initiation buffer (20 mM Tris–HCl [pH 7.5], 50 mM NaCl, 250 μM $MgCl_2$, 1 mM DTT and 5% glycerol), 0.15 μCuries/μl ^{32}P ATP, 20 μM each of unlabeled ATP/CTP/GTP, and 0.01 U/μl *Escherichia coli* RNA polymerase holoenzyme. Reactions were incubated at 37°C for 15 min for elongation, then transferred to ice for 2 min. For synchronized transcription at each condition, 10 μl of stalled RNA polymerase was mixed with 1.5 μl 10× metal solution, and 1.5 μl 10× elongation buffer (4.5 mg/ml, 650 μM each of unlabeled ATP/CTT/GTP/UTP, 100 mM Tris [pH 7.5], 2 mM DTT, 10% glycerol and 2 mM $MgCl_2$. Reactions were incubated at 37°C for an additional 15 min, then terminated by addition of 10 μl RNA loading dye (95% formamide, 20 mM EDTA [pH 8.0], supplemented with xylene cyanol). Transcripts (10 μl) were separated by 6% urea denaturing PAGE and analyzed by a phosphorimager. The sizes of the terminated and full-length RNA products were confirmed by RNA ladder (data not shown). Bands were quantified with ImageJ and each reaction was converted to the fraction of full-length product over total RNA transcribed. The data were fit using Origin 8 data analysis software to the Hill equation ($n = 1$), where x is the concentration of metal and k is the concentration at which the change in read-through is half maximal. Each assay was performed in triplicate.

Statistical analysis

When appropriate, *P*-values were determined relative to non-stressed parent or WT type strains using unpaired t-tests or a one-way ANOVA with Dunnett's post-test determined by GraphPad Prism software.

RESULTS

The *S. pneumoniae mgtA* riboswitch is comprised of a three-way helical junction that is conserved among *Streptococcus* spp.

As described above, the crystallographic structure of the Mn^{2+} bound *L. lactis yaoB* 5′ UTR (*yybP-ykoY* family) aptamer domain reveals a four-way helical junction (4WJ) comprising of tandem coaxially stacked helices (P2 on P1 and P4 on P3) with the two 'legs' of the H-like structure docked at a conserved interface between loop (L) L1 and L3 (Figure 1A) (28). A single Mn^{2+} ion (M_B) is coordinated by six inner-sphere interactions from nucleotides in loops L1 and L3 including an A41 N7-Mn^{2+} coordination bond; a Mg^{2+} ion is also found nearby in M_A (28) (Figure 2). The binding of a single Mn^{2+} ion influences stability of the *L. lactis yaoB* riboswitch like that of a fluoride-sensing riboswitch (44) but in a way that is distinct from the Mg^{2+}-sensing riboswitch (or M-box), in which multiple Mg^{2+} ions cooperatively impact the stability of the riboswitch (45,46).

The *yybP-ykoY* family riboswitch located upstream of the *mgtA* gene in *Streptococcus pneumoniae* D39 reveals, in contrast to the *L. lactis* structure, a three-way helical junction (3WJ) with P4 replaced by an invariant UNAAA (N, can be U or G) sequence (Figure 1B; Supplementary Figure S1C) followed by a transcription termination hairpin with a U-rich sequence (Supplementary Figure S1A). This UNAAA sequence is also found close to a 3WJ in the twister ribozyme (AUAAA), where it induces a sharp turn in the backbone at a helical junction (47). The 5′ end of L1 loop is highly conserved, while the 3′ end contains an invariable AGA nucleotide sequence (nucleotides 101–104) preceded by a variable nucleotide at position 101 that is only conserved as a guanosine among *Streptococcus spp* (Figure 1B; Supplementary Figure S1C). These nucleotides are anticipated to contribute to the metal binding pocket of L1 and L3 in the *mgtA* riboswitch. The metal coordinating nucleotides C49 and A50 as defined by the previous structural work as C49 and A41 in the *L. lactis* RNA (Figure 2) (28,30) within the L3 bulge are also invariant. Finally, the C46-G83 base-pair in the P3.1 stem above L3 is anticipated to hydrogen bond to A18 to form a cross-helix A minor interaction as in other *yybP-ykoY* family riboswitches (Figure 1).

Mn^{2+} and Ca^{2+} to the *mgtA* riboswitch alters an RNA conformational equilibrium

A comparison of the *E. coli mntP* riboswitch in the divalent metal-bound and metal-free (Na^+ only) apo states suggest that the aptamer domain is pre-organized into a conformation that is quite close to the metal-bound form (Supplementary Figure S2), with major differences occurring in L3, which is largely unstructured in the absence of metal (28). The extent to which this is true in solution, however, and for this particular riboswitch specifically, is unclear. To address this, we monitored the folding equilibrium of the *S. pneumoniae mgtA* riboswitch aptamer domain by native PAGE, evaluating the impact of divalent metal cations Mn^{2+}, Ca^{2+} and Mg^{2+} (Figure 3).

In these experiments, the RNA aptamer domain was denatured and refolded at room temperature in a stepwise progression by first adding a monovalent salt (50 mM NaCl), followed by divalent metal cation. Two conformations were resolvable by native PAGE run with Mg^{2+} in the running buffer: an extended or open form (E, upper band) and a more compact form (C, lower band) (Figure 3A). In the absence of added salt, the majority of the RNA (≥80%) is found in the extended form, while inclusion of the 50 mM monovalent salt drives the RNA towards a compacted form. Addition of 1 mM Mg^{2+} to 50 mM Na^+ shifts the equilibrium further to the compacted form but not completely (Figure 3A). The addition of as little as 0.5 mM Mn^{2+} is efficient at compacting the RNA with ≈90% of the RNA adopting the compact form (Figure 3A and Supplementary Figure S3A). As anticipated from a cation competition model, the aptamer appears to fold less efficiently when 1 mM Mg^{2+} and 0.5 mM Mn^{2+} are simultaneously added into the folding buffer relative to folding in the presence of Mn^{2+} alone (Figure 3A). Indeed, nucleotides in L1 and L3 of the *L. lactis yaoB* riboswitch can coordinate binding of either Mn^{2+} or Mg^{2+} (28). The degree to which increasing concentrations of Mn^{2+} shifts the conformational equilibrium to a compact conformation can be modelled assuming that the apo form in 3 mM Mg^{2+} exists as a mixture of extended and compact and Mn^{2+}-bound form is exclu-

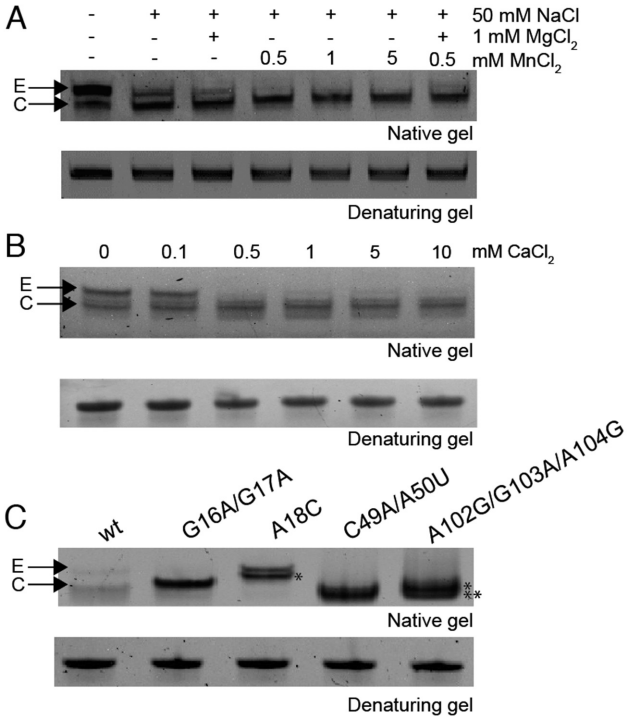

Figure 3. Mn^{2+} or Ca^{2+} binding to *S. pneumoniae mgtA* riboswitch induces conformational change and promotes compact folding. Global hydrodynamic analysis of the RNA aptamer in the presence of metal ions by native-PAGE. (**A**) Influence of salt solution, Mg^{2+} and Mn^{2+} on folding of the wild-type RNA aptamer domain. (**B**) Influence of Ca^{2+} in a background of 0.5 mM NaCl. (**C**) Effects of key metal-binding nucleotides in L1 and L3 that contribute to the overall global structure and compaction of the RNA in a background of 0.5 mM NaCl. Representative gel is shown from at three independent experiments. E, extended form; C, compact form; * and ** denote the two independent folded conformations for the triple mutant RNA, where * is a new conformation.

sively compact. This model of the relative concentrations of the two different RNA conformers gives an effective equilibrium dissociation constant (K_d) of 0.14 ± 0.02 mM (Supplementary Figure S3A and B) in 3 mM Mg^{2+}, or ≈6-fold weaker than that reported for *L. lactis yaoB* riboswitch (K_d of 25 μM for Mn^{2+}) using isothermal titration calorimetry (ITC) in a background of 5 mM Mg^{2+} (30). Quantitative ITC data for the binding of the pneumococcal *mgtA* riboswitch aptamer to divalent cations is presented below.

Although the likely cognate metal ion for the *S. pneumoniae mgtA* riboswitch is Mn^{2+} given its classification as a *yybP-ykoY* family riboswitch, the *mgtA* riboswitch incorporates the ribosome binding site of the *mgtA* gene, which encodes P_{II}-type ATPase transporter (MgtA) that has been implicated in Ca^{2+} efflux (31); furthermore, biophysical experiments show that the analogous transporter from *Listeria monocytogenes* (LMCA1) transports Ca^{2+} (48). Ca^{2+} binding to this family of RNAs has not yet been investigated. Using native-PAGE, we show that 0.5 mM Ca^{2+} also affects the global hydrodynamics of the RNA aptamer, driving the RNA to the more compact form that is similar in mobility to that obtained upon incubation with Mn^{2+} (Figure 3B).

Mutant *mgtA* riboswitch aptamers have altered structures or altered Mn^{2+} sensitivities

To assess which nucleotides coordinate Mn^{2+} in the *S. pneumoniae mgtA* RNA aptamer, we mutated conserved nucleotides in L1 and L3 that comprise the metal binding site region as detailed in other *yybP-ykoY* structures (Figure 2) and tested the impact of these substitutions on the RNA aptamer folding equilibrium by native-PAGE (Figure 3C). These include G16, G17 and A18 on the 5′ side of L1, C49 and A50 in L3 and A102, G102 and A104 on the 3′ side of L1 (*S. pneumoniae* numbering) (see Figure 1B). The G16A/G17A and C49A/A50U RNAs show no change in electrophoretic mobility by native-PAGE over the same range of Mn^{2+} concentration that stabilizes the compacted (C) form of the wild-type RNA (Figure 3C and Supplementary Figure S3C and D), suggesting a loss of Mn^{2+} binding ability. We note that the G16A/G17A mutant RNA appears to migrate slightly faster than the extended (E) form of the WT RNA (Figure 3C). Although the C49A/A50U mutant has lost its ability to bind metal (Supplementary Figure S3D), this mutant RNA migrates similarly with the compacted WT RNA. The triple A102G/G103A/A104G (L1) mutant RNA, on the other hand, simultaneously adopts two RNA conformations that migrate closely with that of the compacted WT RNA, but each is formed independent of Mn^{2+} concentration (Supplementary Figure S3E, Figure 3C). Finally, targeting the predicted cross-strand A-minor interaction (nucleotide A18; Figure 1B) with a cytosine substitution (A18C) shifts the E-to-C equilibrium far toward E, as expected, in a background of 3 mM Mg^{2+} (Supplementary Figure S3F and G) while also increasing the apparent K_d for Mn ≈6.5-fold to 0.90 ± 0.01 mM.

Thus, all four mutant RNAs perturb the RNA conformational ensemble, at least as observed by native-PAGE, and only one of four RNAs (A18C) is responsive to the presence of Mn^{2+}, albeit at much higher metal concentrations. These data suggest that Mn^{2+} binding may not be required to globally fold the *S. pneumoniae mgtA* riboswitch aptamer into an 'X-like' or undocked structure in the presence of physiological (low mM) Mg^{2+}, as all mutant RNAs adopt an E- or E-like state, a finding consistent with recent single-molecule FRET experiments (49).

SHAPE (selective 2′-hydroxyl acylation analyzed by primer extension) probing of the wild-type aptamer

The impact of divalent metal binding on the structure of the *S. pneumoniae mgtA* RNA aptamer was further investigated by the structural probing method SHAPE. SHAPE experiments measure the relative rates of reactivity of 1-methyl-7-nitroisatoic anhydride (1M7) to 2′-hydroxyls and generally report on local flexibility of an individual nucleotide. In the absence of divalent metal (50 mM Na^+ only), nucleotides in L1 (16–21; 102–104) and L3 (residues 48–50) show high to moderate reactivity (Figure 4A), suggesting that no metal-binding pocket is formed. A18 of the A-minor interaction is also moderately flexible in the absence of metal ions. The addition of Mg^{2+} stabilizes base-pairing in the P2 stem (residues 28–29), destabilizing the base of the P3.2 stem, while quenching flexibility of all nucleotides implicated in metal binding, including both sides of L1 and C49 and A50 in L3 (Figure 4B). The modest reduction in flexibility observed for nucleotides A18 in L1 and C49 and A50 in L3 suggests that the A-minor interaction forms in the presence of Mg^{2+} alone. Addition of Mn^{2+} to a background of Mg^{2+} leads only to a small change in the flexibility of nucleotides C49 and A50, which are predicted to directly interact with the Mn^{2+} M_B ion (*vide infra*), making them more rigid (Figure 4C). The addition of Ca^{2+} results in a SHAPE profile (Figure 4D) that is statistically indistinguishable from that obtained upon addition of Mn^{2+}. These data taken together reveal that the RNA conformation obtained in the presence of the 3 mM Mg^{2+} alone, Mg/Mn and Mg/Ca are very similar and that major differences in reactivity relative to the Na^+-only structure are localized to the metal-binding region. These findings are consistent with native-PAGE analysis which reveals roughly two distinct conformations with distinguishable, yet rather similar, electrophoretic mobilities.

Small angle X-ray scattering (SAXS) analysis of *mgtA* riboswitch aptamers

Small angle X-ray scattering (SAXS) was next used to obtain additional insights into the global fold of the wild-type *mgtA* RNA as a function of divalent metal ion status, compared to the G16A/G17A L1 mutant which fails to adopt the compact or *C*-state. Refolding of the aptamer in buffer with NaCl only and no divalent metal ions results in the largest radius of gyration (R_g) (Supplementary Figure S4; ≈37 Å) with clear evidence of conformational heterogeneity in this state. Addition of Mg^{2+} results in a significant increase in RNA compaction, with the R_g some 10 Å smaller, to 26.7 ± 0.5 Å. Addition of Mn^{2+} to the Mg^{2+}-folded structure results in a similarly compacted structure, that is perhaps slightly more extended (R_g = 27.6 ± 0.4 Å) with no significant change observed with the addition of Ca^{2+} to

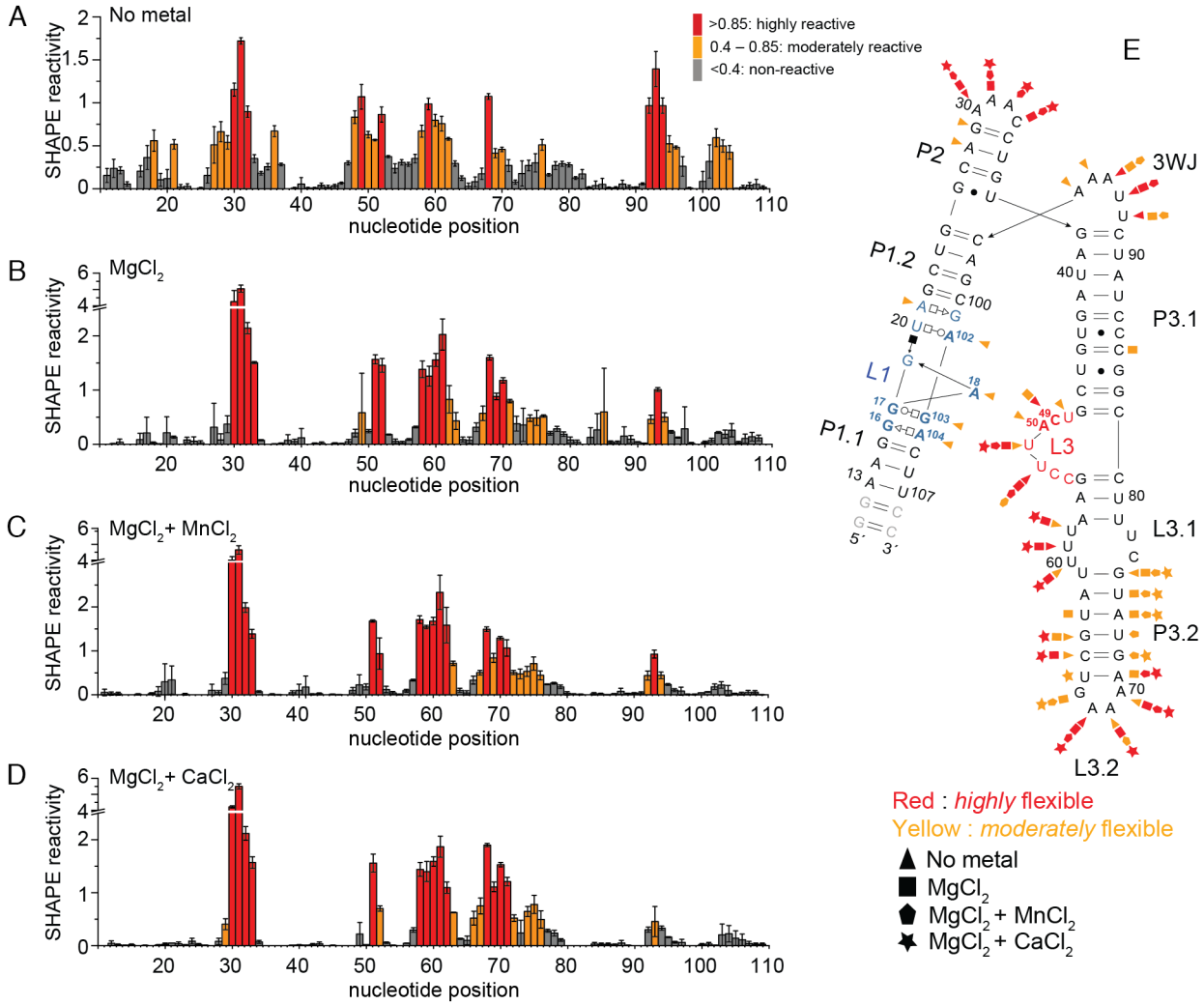

Figure 4. Mn^{2+} and Ca^{2+} impact nucleotide flexibility in the *mgtA* RNA aptamer. (**A**) SHAPE reactivity of the *S. pneumoniae mgtA* RNA aptamer domain in the presence of various divalent metals. Regions of low reactivity (<0.4) are colored *gray*, moderate reactivity (0.4–0.85) are *yellow*, and high reactivity (>0.85) are *red*. Each bar represents a single nucleotide in the sequence as numbered on x-axis. (**B**) Summary of the flexibility of nucleotides in the RNA aptamer.

the Mg^{2+} folded RNA. The dimensionless Kratky plots also reveal that the *mgtA* aptamer folds upon the addition of Mg^{2+}, while inclusion of other transition metals tested only change the overall compaction of the RNA slightly (Figure 5A and B). A significant change in the pair-wise distance distribution is observed with Mg^{2+} showing a larger number of shorter distances (20–40 Å) within the RNA (Figure 5C), consistent with a folded form of the *mgtA* aptamer RNA. Only a minor change in the pair-wise distance distribution results when Mn^{2+} or Ca^{2+} are present in a background of Mg^{2+} (Figure 5C). Taken together these data are consistent with the native-PAGE and SHAPE results, demonstrating that different divalent metal ions can lead to conformational change and compaction of the *mgtA* RNA aptamer.

We next used these data to calculate a three-dimensional (3D) envelope (or bead model) of the *mgtA* RNA aptamer, which could only be determined in the presence of divalent metal ions, a finding consistent with the conformational heterogeneity in the metal-free form of the RNA as evidenced by the non-linear Guinier plot (Supplementary Figure S4A). As expected, the resulting averaged envelopes obtained in the presence of Mg^{2+} plus Mn^{2+} or Mg^{2+} plus Ca^{2+} are similar (Figure 5D and E), but yet distinct from that of Mg^{2+} alone (Figure 5F). A simulated structural model of the aptamer embedded into the SAXS envelope in the presence of Mg^{2+}/Mn^{2+} or Mg^{2+}/Ca^{2+} fits well (Figure 5D), showing that in the presence of Mn^{2+} or Ca^{2+}, the three hairpins likely organize into two coaxially stacked helices (P2 on P1) connected to a third helix (P3) at the three-way junction (3WJ).

In contrast to the WT RNA aptamer, the non-metal binding G16A/G17A mutant RNA that fails to adopt the compact form at any Mn^{2+} concentration by native-PAGE analysis (Supplementary Figure S3C) adopts a more extended average conformation ($R_g = 29.3 \pm 0.4$ Å), independent of Mn^{2+} (Figure 5B and C). The resulting averaged SAXS-derived bead model yields a 'Y-like' topology, suggesting that the G16A/G17A mutant RNA is characterized by an

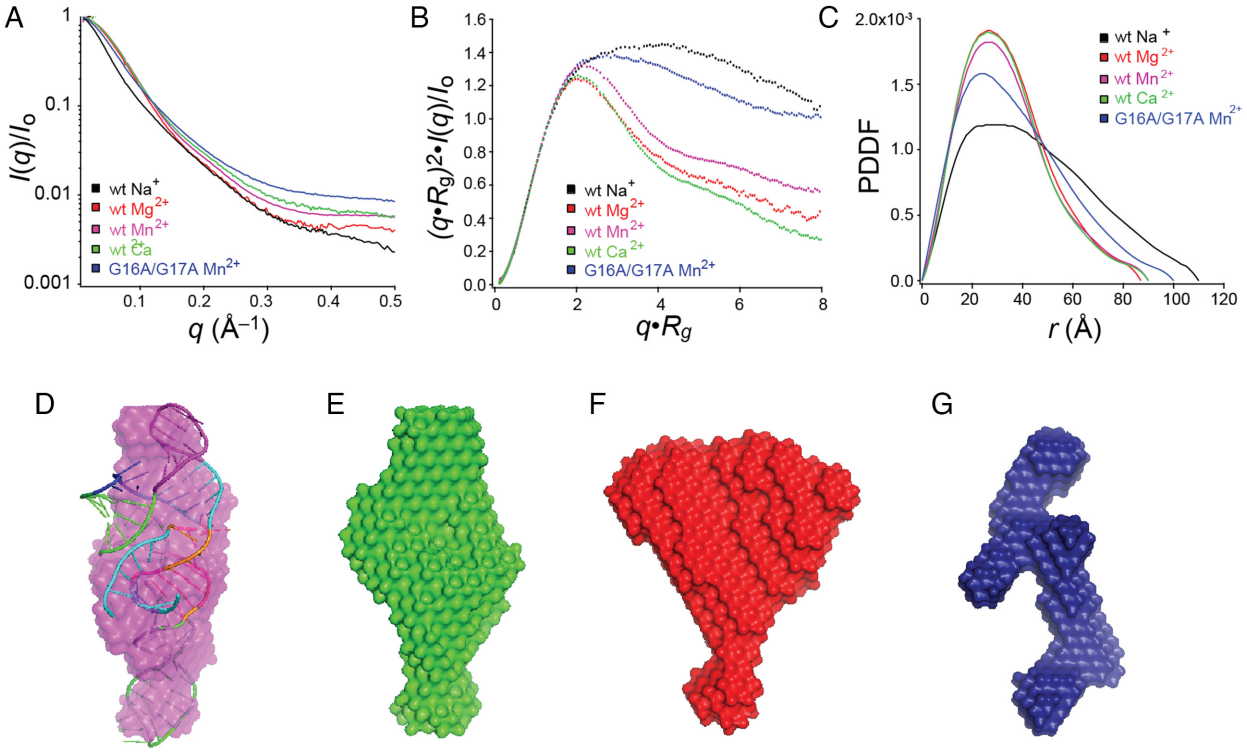

Figure 5. Global structure analysis of the *mgtA* RNA aptamer with divalent metal ions. (**A**) Scattering profiles collected at separate RNA concentrations 0.8, 1.6 and 3.2 mg/ml with indicated metal, then merged. (**B**) Dimensionless Kratky plots. (**C**) Pair-wise distance distribution plots for all RNAs. (**D**) Simulated 3D structure of the RNA aptamer by SimRNA embedded in the envelope obtained from SAXS in the presence of Mn^{2+}. SAXS simulated envelope models for WT RNA with Ca^{2+} (**E**), Mg^{2+} (**F**) and the G16A/G17A mutant RNA that is unable to bind metal (**G**).

open or extended conformation minimally comprising three helices connected by a 3WJ (Figure 5G).

The mgtA riboswitch aptamer binds Ca^{2+} more tightly than Mn^{2+}

The genomic location of the *S. pneumoniae mgtA* riboswitch as well as our own hydrodynamic data (Figures 3–5) suggest that Mn^{2+} and possibly Ca^{2+} may be regulatory. We next used ITC to monitor the binding of Mn^{2+} and Ca^{2+} directly, monitored at what we anticipate is near physiological conditions of Mg^{2+} (3 mM). The binding of Mn^{2+} to the *mgtA* RNA aptamer is exothermic, whereas the binding of Ca^{2+} is endothermic, where Mn^{2+} binding is more strongly entropically-driven relative to Ca^{2+} (Figure 6 and Table 1). Both metals bind to the *mgtA* riboswitch with an apparent stoichiometry, *n,* ≈1, likely reporting on the displacement of Mg^{2+} bound to the M_B site by Ca^{2+} or Mn^{2+} (Figure 2A) (28). The effective K_d for Ca^{2+} is low micromolar (1.72 ± 0.03 μM), which is 50-fold higher affinity than for Mn^{2+} ($K_d = 54 \pm 26$ μM). The K_d for Mn^{2+} obtained from ITC is somewhat tighter than that derived from native-PAGE folding equilibrium analysis, although both are in the 10^{-4} M Mn^{2+} range (Supplementary Figure S3A and B).

A significant number of the structural models of metal-bound *yybP-ykoY* riboswitches have been reported and are often used to interpret the sensing mechanism of riboswitches (Figure 2B and C). Moreover the recent reported affinities for Cd^{2+}, K_d in the sub-mM range depending on the construct (30), suggest that Cd^{2+} could potentially turn on the *yybP-ykoY* riboswitches. To test the significance of those models in the context of the *mgtA* riboswitch, we also determined Cd^{2+} binding to the *mgtA* riboswitch. Although the *mgtA* RNA aptamer is compacted in the presence of 500 μM Cd^{2+} in a background of 3 mM Mg^{2+} (Supplementary Figure S5A), higher concentrations of Cd^{2+} drive the RNA aptamer into a more slowly migrating conformation(s) by native-PAGE. This suggests that at low concentrations, Cd^{2+} may bind in the same pocket (M_B) (see Figure 2B) as Mn^{2+} and Ca^{2+}. Both SHAPE (Supplementary Figure S5C) and SAXS (data not shown) analyses suggest that an extended or more open conformation is formed at high Cd^{2+} concentrations. It is also worth noting that low Cd^{2+} concentrations (≤500 μM) fail to activate

Table 1. Thermodynamic parameters of cation interactions with the *mgtA* RNA aptamer

Parameter[a]	Mn^{2+}	Ca^{2+}
K_d (μM)	54 ± 26	1.72 ± 0.03
n	1.0 ± 0.0	1.07 ± 0.0
ΔH (kcal/mol)	1.1 ± 0.1	–3.6 ± 0.1
$T\Delta S$ (kcal/mol)	7.0 ± 0.2	4.3 ± 0.1
ΔG (kcal/mol)	–5.9 ± 0.02	–7.9 ± 0.2

[a]Mean and standard deviations are obtained from duplicated independent experiments. All experiments were performed in a background of 3 mM $MgCl_2$ at 25°C. Data reported here are calculated from a one-site random binding model.

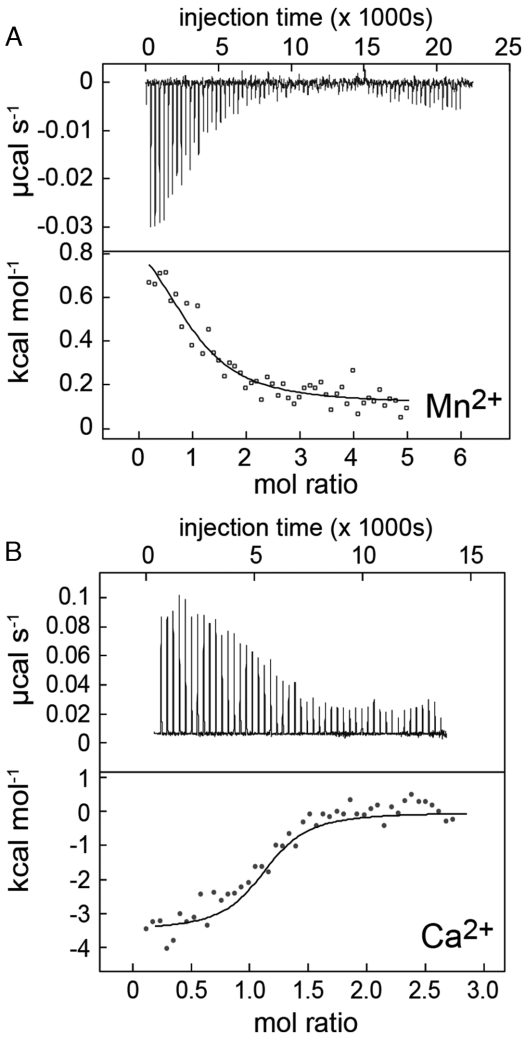

Figure 6. Thermograms of the interaction of the *mgtA* aptamer with Mn^{2+} (**A**) or Ca^{2+} (**B**) by isothermal titration calorimetry. For each panel, the upper panel shows the raw ITC data plotted as the change in power ($\mu cal\ s^{-1}$) required to maintain equal temperature between the sample and reference cells as the function of time; lower panel shows intergated heat normalized for mol of injectant added. The thermodynamic parameters for metal binding defined by the continuous lines drawn through the data are summarized in Table 1.

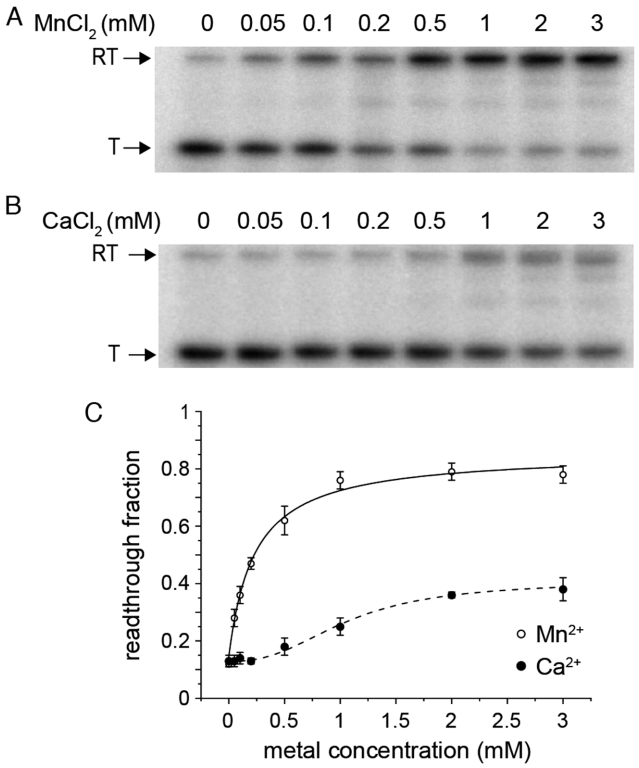

Figure 7. Mn^{2+} activates *in vitro* transcription of *mgtA* better than Ca. ^{32}P labeled products produced in presence of Mn (**A**) and Ca (**B**) (in a background of 250 µM Mg^{2+}) were separated by PAGE. Termination (T) products reflect terminator formation. Read-through (RT) products form as a result of metal-binding and stabilizing the aptamer thereby preventing formation of the terminator. (**C**) Quantification of *in vitro* transcription termination assays, with the continuous lines fit to a Hill model of activation (see text for details).

transcription read-through and that higher Cd^{2+} concentrations are inhibitory (data not shown). Collectively, these data suggest that Cd^{2+} can bind and affect global change of the *mgtA* riboswitch, however the functional outcome is not likely physiologically relevant.

The *mgtA* riboswitch responds more robustly to Mn^{2+} *in vitro*

Previously, it was demonstrated by *in vitro* transcription (IVT) termination experiments that the *L. lactis yaoB* riboswitch is activated by 0.5 mM Mn^{2+} but not by other metal ions tested (Fe^{2+}, Co^{2+}, Ni^{2+} and Ca^{2+}); Mg^{2+} also induced transcription read-through, but only when provided at high concentrations (10 mM), suggesting that Mg^{2+} is not a preferred metal (28). Likewise, an *L. lactis yaoB* riboswitch chimera harboring L3 mutations to match the *E. coli mntP* and *alx* riboswitch L3 nucleotides, respond to Mn^{2+} as do other transition metals tested (Cd^{2+}, Co^{2+}, Cu^{2+}, Fe^{2+} and Ni^{2+}); however, transcription read-through was not induced by Ca^{2+}, Mg^{2+} and Zn^{2+} (30). Other experiments demonstrate that these *yybP-ykoY* family riboswitches can also mediate Mn^{2+}-dependent regulation *in vivo* (28,29). Thus, it is not possible to predict which metal induce transcription for the *mgtA* RNA aptamer based solely on it being part of the *yybP-ykoY* family riboswitches, nor on the selectivity in terms of binding for different metal ions. This observation motivated a series of *in vitro* transcription termination assays to determine which metal induces transcription for the *mgtA* RNA.

The binding of Mn^{2+} to the *S. pneumoniae* RNA aptamer is hypothesized to destabilize the terminator hairpin and permit read-through transcription of full-length *mgtA* mRNA transcript (Supplementary Figure S1C). Indeed, titration of increasing Mn^{2+} concentrations into the reaction led to the synthesis of full-length transcripts by *E. coli* RNA polymerase (Figure 7A) in a background of 250 µM Mg^{2+}, revealing that Mn^{2+} binding to the aptamer activates transcription read-through. Ca^{2+} is also capable of activating transcription read-through (Figure 7B), but to a much lower extent compared to Mn^{2+} (Figure 7C). The half-maximal transcriptional activation by Mn^{2+} (0.23 ±

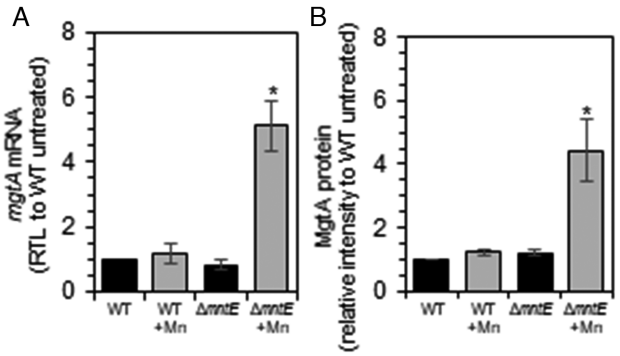

Figure 8. *mgtA* is induced during Mn-stress. Exponentially growing *S. pneumoniae* cells were diluted into pre-warmed BHI broth with 0 (*black*) or 200 μM (*gray*) Mn. Cells were harvested after 3.5 h growth. (**A**) Relative transcript levels of *mgtA* RNA. (**B**) Relative intensities of FLAG-tagged MgtA protein. The mean of at least three independent cultures ± SEM are shown. **P*-value ≤ 0.05.

0.1 mM; Hill number, $n_H = 1$) reveals that 5-fold less Mn^{2+} is needed to activate transcription read-through when compared to Ca^{2+}, which is half-maximal at 1.1 ± 0.1 mM; Hill $n_H = 2.5 \pm 0.6$. Thus, despite the fact that Ca^{2+} binds more tightly to the RNA aptamer than Mn^{2+} (Figure 6) and appears to yield a similar conformation in solution, it stimulates read-through transcription to a far lesser degree. We found that Mg^{2+} alone is also capable of stimulating transcription read-through of *mgtA* (Supplementary Figure S6) with the addition of 3 mM Mg^{2+} resulting in ≈50% maximum read-through (Supplementary Figure S6B), yielding an effective K_d of 1.7±0.8 mM (Hill $n_H = 1.0 \pm 0.8$). Thus, Mn^{2+} is the most effective activator of *mgtA* transcription read-through and is uniquely functional at sub-mM Mn^{2+} in a concentration range comparable to the K_d^{Mn}.

The *S. pneumoniae mgtA* riboswitch responds more robustly to Mn^{2+} *in vivo*

We next determined if the *S. pneumoniae mgtA* riboswitch could also mediate Mn^{2+}- and Ca^{2+}-dependent regulation *in vivo*. *S. pneumoniae* cells lacking the Mn-specific exporter MntE (encoded by *mntE*) were used to induce Mn-stress growth conditions; Δ*mntE* cells accumulate high levels of intracellular Mn compared to wild type (WT) cells (34,50). During cellular Mn stress, *mgtA* mRNA and MgtA protein levels increase 5- and 4-fold, respectively, for Δ*mntE* mutants compared to WT cells (Figure 8 and Supplementary Figure S7). Clotrimazole, known to inhibit Ca^{2+} transport of eukaryotic sarco/endoplasmatic reticulum Ca^{2+}-ATPase (SERCA P_{II}-type ATPase), served as a suitable agent for imposing Ca^{2+}-stress in *S. pneumoniae* WT cells (Supplementary Figure S8A). We note that clotrimazole treatment did not significantly affect intracellular Mn levels (Supplementary Figure S8B). We found that MgtA protein synthesis remained unchanged during Ca^{2+}-stress, despite a 4-fold increase in cellular Ca^{2+} levels (Supplementary Figure S8C). No further metal activation studies were performed in *S. pneumoniae*, since we subsequently discovered that deletion of *mgtA* and possibly lower cellular MgtA protein levels are detrimental to cell viability (see below).

As an alternative method, we fused the *S. pneumoniae mgtA* leader region containing the *mgtA* riboswitch to a *lacZ* gene and monitored metal activation in *Bacillus subtilis* WT and Δ*mntR* strains. The latter strain experiences Mn toxicity, because the Mn-repressor MntR coordinates transcriptional regulation of the Mn uptake transporters (MntH and MntABC) and the Mn efflux pumps (MneP and MneS) (51,52). In the *B. subtilis* Δ*mntR* strain, the *mgtA-lacZ* mRNA level increases several-fold with the addition of Mn^{2+} to the growth medium (Figure 9A). Likewise, increasing Mn^{2+} concentrations stimulates expression of β-galactosidase up to 3.5-fold (*black* solid circles, Figure 9B). Removal of the terminator hairpin led to significantly higher activity (*red* solid squares), while deletion of the aptamer domain resulted in a minimal change in activity (*grey* solid triangles, Figure 9B). No response was observed in the absence of the 100 nt region upstream of the predicted *mgtA* riboswitch (open symbols, Figure 9B).

In contrast to Mn^{2+}, the addition of other metal ions (Zn^{2+}, Cu^{2+}, Fe^{2+}, Ni^{2+}, Co^{2+}, Mg^{2+} or Ca^{2+}) to the growth medium had little to no effect on β-galactosidase expression (Figure 9C). Again, no response was observed in the absence of the 100 nt region upstream of the aptamer (Supplementary Figure S9). Deletion of the transcriptional terminator hairpin led to several-fold higher activation, while loss of the aptamer domain showed little if any change (Figure 9C). In *B. subtilis* WT cells, ≥400 μM Mn^{2+} was required to observe activation of β-galactosidase expression (Figure 9D). No activation was observed in WT cells with other metal ions tested (Supplementary Figure S9B), including Ca^{2+} (Figure 9D) even when added up to 10 mM (data not shown). Together, these data demonstrate that the *S. pneumoniae mgtA* riboswitch functions as a Mn^{2+}-specific 'on' switch *in vivo*, inducing expression of MgtA.

To further connect aptamer folding with function and confirm metal specificity *in vivo*, key nucleotides within the *S. pneumoniae mgtA* RNA aptamer shown to disrupt folding of the aptamer were mutated in the context of the 5′ UTR and tested for functionality *in vivo* in a heterologous *B. subtilis* expression system. Both L1 (G16A/G17A) and L3 (C49A/A50U) substitutions reduced expression of β-galactosidase for all metal ions tested (Figure 9E). In contrast, the triple mutation of the 3′ side of L1 (A102C/G103A/G104G) results in high-level expression for all metals tested except for Zn^{2+} and Cu^{2+}, which inhibit growth under these conditions, to a level consistent with unregulated expression, i.e. that obtained with aptamer alone (Figure 9C). This mutant 5′ UTR RNA may mis-fold in the cell and lead to a loss or destabilization of the terminator hairpin (see Supplementary Figure S1B). Taken collectively, these data correlate well with our global conformational analyses (Figures 3–5).

The *mgtA* riboswitch regulates a P_{II}-type ATPase that protects cells against Mn toxicity

Our results so far indicate that the *S. pneumoniae mgtA* riboswitch functions as a Mn^{2+}-specific sensor that turns on a predicted P_{II}-type ATPase metal effluxer, MgtA, that we reasoned might play a role in cellular Mn homeostasis. To investigate this, we constructed *S. pneumoniae* D39

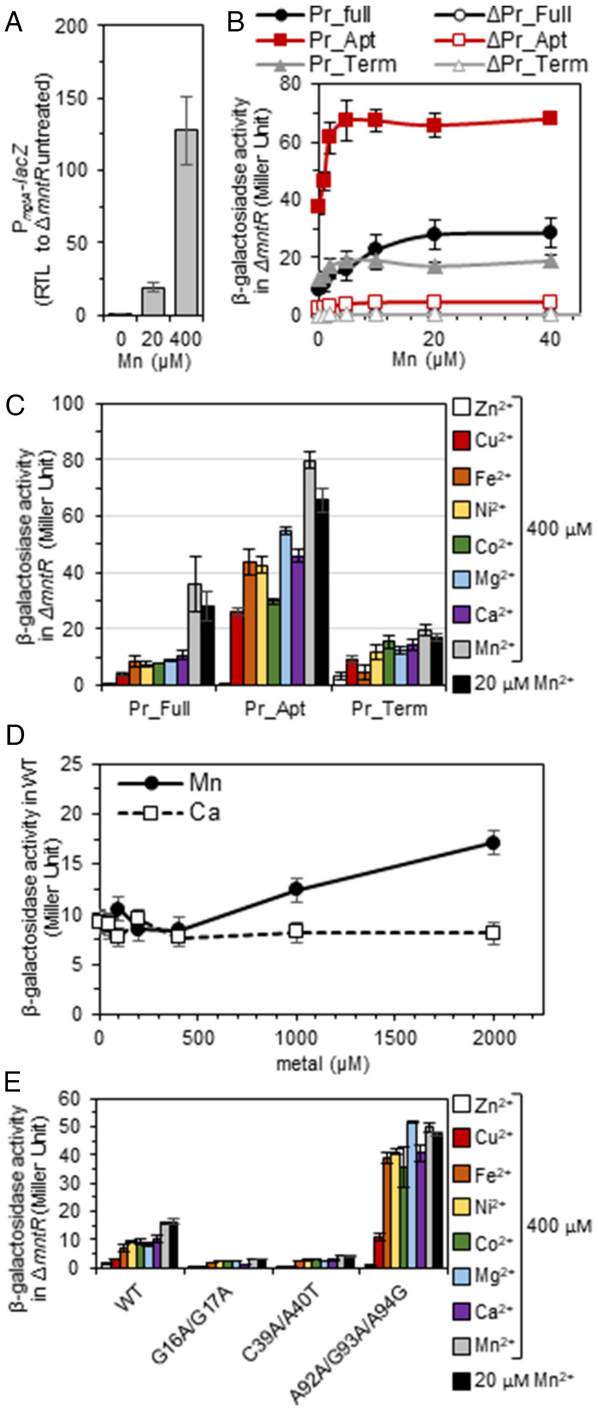

Figure 9. The *S. pneumoniae mgtA* riboswitch senses and responds specifically to intracellular Mn in *B. subtilis*. Exponentially *B. subtilis* cells growing in LB treated with indicated metal for 2 h, then harvested. (**A**) Relative transcription of P_{mgtA}-*lacZ* fusion in Δ*mntR* cells grown with increasing concentrations of Mn. (**B**) β-Galactosidase activity in Δ*mntR* carrying various promoter-*lacZ* fusions in response to increasing concentrations of Mn. (**C**) β-galactosidase activity in response to various metal cations. (**D**) β-Galactosidase activity in WT cells containing WT-*mgtA* leader sequence in response to Mn and Ca. (**E**) β-galactosidase activity in Δ*mntR* carrying Pr_full (WT) and mutant forms the *mgtA* riboswitch in response to various metal cations. The mean of at least three independent cultures ± SEM are shown. Pr_Full, promoter plus intact 5′ UTR (185 nt; see Supplementary Figure S1); Pr_Apt, promoter plus aptamer (nucleotides 1–124); and Pr_Term, promoter plus terminator hairpin (nucleotides 101–185).

strains harboring clean deletions of *mgtA* and *mntE*, singularly or in combination. Transformation efficiency for the Δ*mgtA* strain appeared typical, despite a two-thirds reduction in colony size, while the Δ*mgtA* Δ*mntE* strain had the lowest efficiency, when selected on TSAII+SBA medium containing antibiotic under 5% CO_2 atmosphere. Colony appearance was uniform in size and shape (data not shown). Absence of oxygen did not improve colony size of Δ*mgtA* mutants during the selection process, suggesting that the colony phenotype was not a result of reactive oxygen species. Furthermore, Δ*mgtA* isolates failed to reach 0.2 OD in 8–12 h when inoculated in brain-heart infusion (BHI) broth. Prolonged growth (>24 h) in BHI yielded fast-growing suppressors in isolated Δ*mgtA* harboring strains. Supplementation of BHI with exogenous Mg^{2+}, Ca^{2+}, Mn^{2+} or Fe^{2+} did not affect the growth pattern observed, nor did treatment with metal chelators EDTA and desferrioxamine (data not shown). These data support the idea that MgtA plays a role in Mn homeostasis in *S. pneumoniae*, since combined Δ*mgtA* and Δ*mntE* mutations showed the most pronounced colony defect during strain construction. We note that a Δ*mgtA* mutation was reported previously in *S. pneumoniae* D39 (53); however, we suspect that suppressor mutations were present in this strain, given the discrepancies with other published papers (25,31).

Because of this apparent requirement for pneumococcal MgtA under metal replete conditions, we tested the ability of MgtA to rescue Mn-sensitivity in a *B. subtilis* Δ*mntR* mutant. The *S. pneumoniae mgtA* gene was placed under an IPTG-inducible promoter and integrated into the chromosome of *B. subtilis* in single copy. Induction of MgtA synthesis has no effect on wild-type cell growth over time in LB with or without Mn (Figure 10A and Supplementary Figure S10). *B. subtilis* Δ*mntR* mutants fail to grow in the presence of Mn^{2+} compared to wild-type cells (Figure 10A and Supplementary Figure S10) due to Mn accumulation (Figure 10B). This Mn sensitivity is largely eliminated by induction of MgtA synthesis (Figure 10A). Total cell-associated Mn levels do not rise in Δ*mntR* mutants when MgtA is overexpressed, despite treatment with exogenous Mn^{2+} (Figure 10A). Interestingly, Ca^{2+} levels are significantly lower only in Δ*mntR* treated with Mn^{2+} only when MgtA is induced (Figure 10B). All other metals (Fe^{2+}, Zn^{2+}, Cu^{2+}) examined remained similar to WT levels (Supplementary Figure S11); Ni^{2+} and Co^{2+} were below the level of detection. These data indicate that the MgtA P-type ATPase transporter is capable of transporting both Ca^{2+} and Mn^{2+} under conditions of extreme Mn^{2+} toxicity. Further studies are required to fully understand the physiological importance of Ca^{2+} transport by MgtA in cells.

DISCUSSION

Metal cation homeostasis is essential for colonization and pathogenesis of bacteria. As such, the mammalian host has evolved mechanisms to both restrict or intoxicate invading bacteria with specific metals, depending on the microenvironmental niche. In response, bacteria have evolved complex regulatory strategies to adapt in an effort to maintain homeostasis of essential metal ions. Recent work provides support for the idea that individual metal ions in a bac-

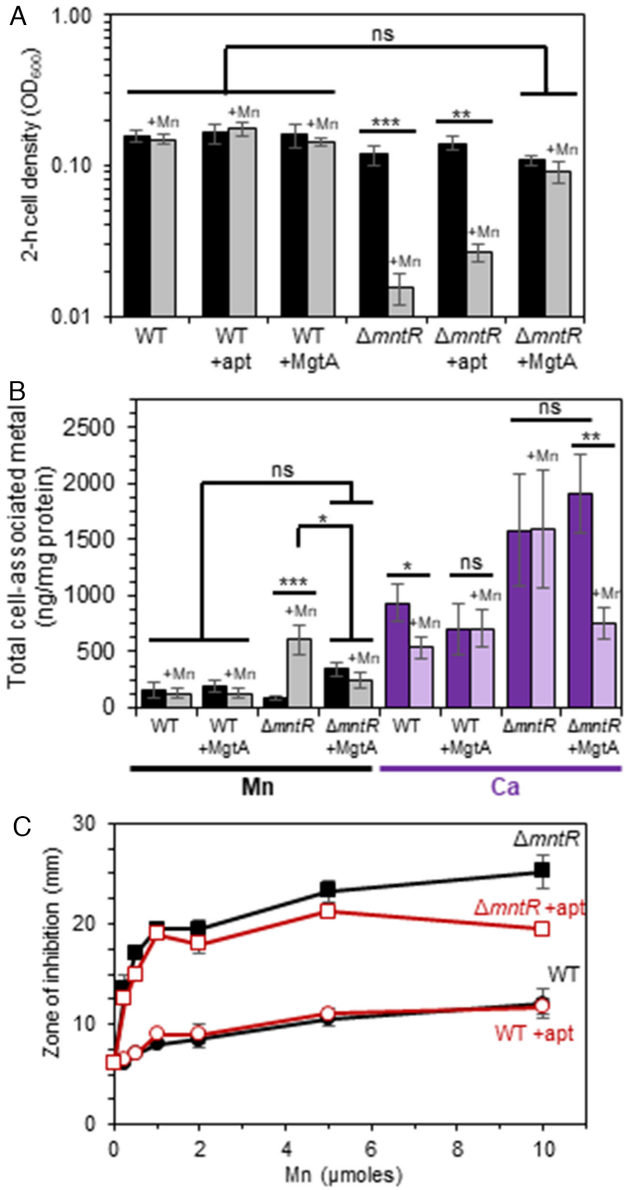

Figure 10. *S. pneumoniae* MgtA protein that is associated with the *yybP-ykoY* riboswitch rescues Mn-sensitivity in *B. subtilis*. Sensitivity of Mn^{2+} was monitored in *B. subtilis* WT and Δ*mntR* cells harboring the *mgtA* RNA aptamer sequence or MgtA in LB broth containing 0 (*darker* bars) or 50 μM (*lighter* bars) Mn overtime. Isopropyl β-D-thiogalactopyranoside (1mM) was added to induce MgtA protein synthesis. (**A**) 2-h cell density. (**B**) Total cell associated Mn and Ca determined by IPC-MS after 2.5 h growth. (**C**) Disk diffusion assay. The mean of at least three independent cultures ± SEM are shown for each experiment. **P*-value ≤ 0.05; ***P*-value ≤ 0.01; ****P*-value ≤ 0.001; ns, no significance.

terial cell are buffered to an extent that is largely determined by the absolute sensitivities or set-points of metallosensors that regulate the expression of downstream genes, which often encode metal transporters (54,55). These metallosensors detect metal activities (free metal concentrations) around a relatively narrow concentration window defined by their K_d^{Me} (Me, metal), a range in concentration that is often far less than total cell-associated metal (54,55). Of importance here is that Mg^{2+} levels are thought to be maintained in the low mM range, primarily controlled by the Mg^{2+}-sensing 'M-box' riboswitch (in *B. subtilis*, for example) (45), while Mn^{2+} concentrations are transcriptionally controlled by Mn^{2+}-sensing protein repressors MntR in *B. subtilis* (56) and a related repressor PsaR, in *S. pneumoniae* (57). The M-box riboswitch is tuned to ≈mM affinity (55). The K_d^{Mn} for the regulatory 'sensing' site in PsaR is in the low μM range (1.3 μM), while the *Salmonella* MntR K_d^{Mn} is about 10-fold lower affinity (13 μM at pH 8.0) (55). This 'set-point' model suggests that Mn^{2+} may be buffered in the low μM range, which in *S. pneumoniae* may be further restricted by the constitutive expression of MntE, to which effluxes Mn^{2+} from the pneumococcal cell (50). In contrast to what is known about Mn^{2+} homeostasis, intracellular bacterial Ca^{2+} homeostasis remains largely unexplored, and to our knowledge a bacterial Ca^{2+}-specific metallosensor or two-component response regulatory system has yet to be described.

In this report, we describe the physical and functional characterization of a Mn^{2+}-sensing riboswitch that is found upstream of the *mgtA* gene. Using a combination of native gel mobility experiments, SHAPE probing, SAXS analysis and *in vitro* transcription experiments, we show that this riboswitch aptamer domain is capable of binding Mn^{2+} and Ca^{2+} in the presence of mM Mg^{2+}, and that all three metals, including Mg^{2+} alone stabilize a compact state, relative to an extended or 'open' conformation. All three metals stimulate transcription read-through *in vitro* using *E. coli* RNA polymerase, but Mn^{2+} is clearly the most potent activating metal in these experiments, both in terms of maximal read-through activity and metal sensitivity (≤100 μM metal). The half-maximal Mn^{2+} concentration required to shift the folding equilibrium of the RNA to the compact form and stimulate *in vitro* transcription is within a factor of four of the K_d^{Mn} measured by calorimetry (50–200 μM); furthermore, the response in all three experiments conducted in 3 mM Mg^{2+} fits well to a rectangular hyperbolic function, consistent with a single Mn^{2+}-sensing site on the riboswitch, which we speculate is the Mn_B site (see Figure 2A). As anticipated from previous work, mutations in the metal-site pocket abrogate or greatly weaken (A18C) Mn^{2+}-dependent folding, and when incorporated into the *mgtA* 5′ UTR in cells, render them functionally inactive.

These physical characteristics are largely recapitulated in pneumococcal cells and in a heterologous *B. subtilis* host, with Mn^{2+} the only divalent metal ion capable of read-through transcription in either cellular background, which in *S. pneumoniae* results in a corresponding increase in the cellular amount of MgtA protein. Ca^{2+} is not a strong *mgtA* inducer *in vivo*. However, significant Mn^{2+}-dependent mRNA or protein expression in either bacterial host is only observed in a strain that is extremely sensitive to Mn^{2+} toxicity, i.e. in Δ*mntR B. subtilis* and in Δ*mntE S. pneumoniae.* Under these conditions where *mgtA* mRNA and MgtA protein levels are higher, MgtA is capable of lowering total cell-associated Mn^{2+}, consistent with a role in Mn^{2+} efflux by MgtA. These physiological findings are entirely consistent with the observed *in vitro* metal sensitivity of the riboswitch itself, which is in the 50–200 μM Mn^{2+} range, or set ≥5–10-fold higher than the metalloregulator proteins MntR and PsaR; unfortunately, the metal binding affinity of the MntE

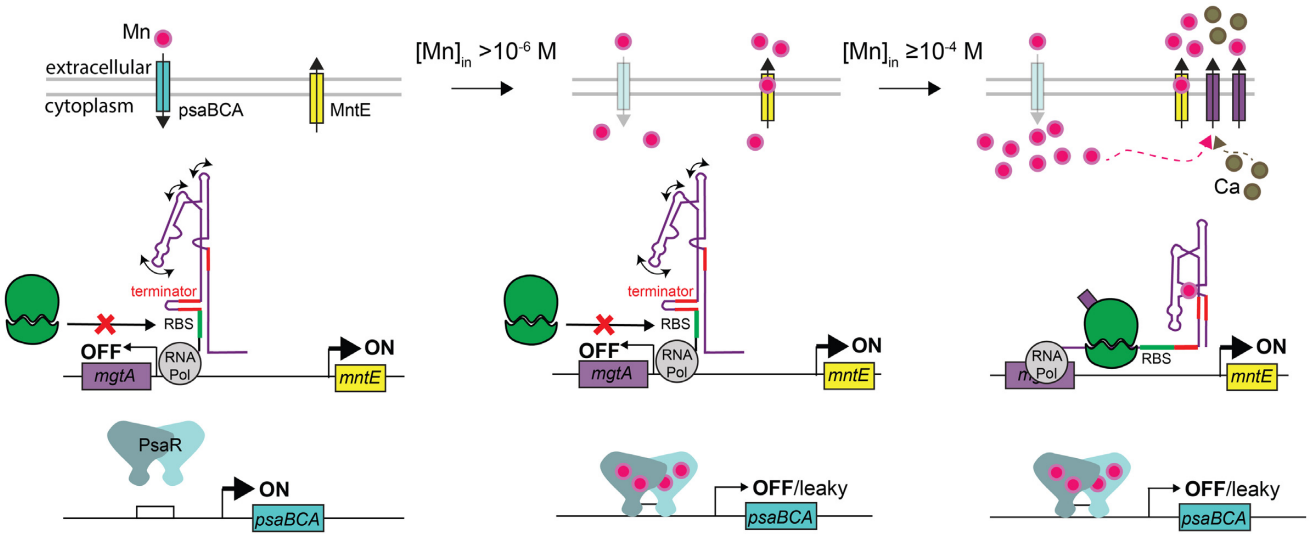

Figure 11. Threshold model for Mn^{2+} sensing and detoxification in *S. pneumoniae*. The Mn^{2+} binding affinity of the *S. pneumoniae mgtA* riboswitch is such that there is sufficient free intracellular Mn^{2+}, governed by the relative affinities of the transcriptional Mn uptake repressor PsaR and the constitutively expressed Mn-specific efflux pump MntE (34,57), to ensure MgtA is not induced and that key intracellular Mn-dependent enzymes are active. At concentrations >1 μM Mn^{2+}, PsaR will bind Mn^{2+}, increasing its affinity to DNA and repress *psaBCA* transcription, thereby reducing Mn import; excess Mn^{2+} will continue to be effluxed by MntE. Our data suggest that as free Mn^{2+} rises to ≥100 μM, the *mgtA* riboswitch functions as a failsafe 'on' signal inducing MgtA expression to prevent Mn^{2+} toxicity. In addition, the riboswitch also functions to regulate Ca^{2+} efflux under this condition.

has not yet been determined but might be expected to be in the low μM range. Thus, if these systems are present and functioning, they would prevent intracellular Mn^{2+} from reaching the ≈100 μM range, and thus this riboswitch and subsequent MgtA protein production would simply not fire. Thus, our data support the hypothesis that the MgtA production functions as a 'fail-safe' or back-up system to allow *S. pneumoniae* to adapt to acute phases of Mn^{2+} toxicity in the host when Mn^{2+} uptake regulated by PsaR and Mn^{2+} efflux by MntE fail to avoid cellular toxicity (Figure 11) (50).

The functional significance of Ca^{2+} binding by this riboswitch and Ca^{2+} efflux by MgtA under conditions of extreme Mn^{2+} stress (Figure 10B) are not yet known. MgtA is clearly capable of effluxing Ca^{2+} from cells and clotrimazole and extracellular Ca^{2+} interfere with this process (Supplementary Figure S8), but under what conditions this might occur during the course of a bacterial infection are not known. *mgtA* is the first gene in a co-transcribed two-gene operon with a downstream, non-essential gene (*spd_1382*) encoding a glutathione S-transferase (25). Consequently, the defective growth of Δ*mgtA* mutants, irrespective of Mn^{2+} status, could be due to a polarity on Spd_1382 expression and/or a second role of MgtA in cellular metabolism possibly in maintaining Ca^{2+} homeostasis. The former is less likely as the replacement of the native *mgtA* gene with a construct encoding MgtA triple-FLAG-tagged protein linked to an antibiotic resistance cassette did not show defective growth (data not shown). The putative essentiality of *mgtA* was not studied further here, but an implication of this operon arrangement is that expression of the Spd_1382 glutathione S-transferase is also controlled by the *mgtA* riboswitch aptamer in response to Mn^{2+} and Ca^{2+}. One possibility is that under metal-replete conditions, small amounts of MgtA produced via leaky expression function in Ca^{2+} efflux, perhaps required to efficiently metallate an obligatory Ca^{2+}-requiring enzyme on the outside of the pneumococcal cell; indeed, such a role for P_{1B}-type ATPases in metallating periplasmic, extracellular or membrane-anchored client proteins is not without precedent for Cu^{+}-specific P_{1B}-ATPases in other bacteria (58–60). Alternatively, MgtA might play an important role in maintaining Ca^{2+} homeostasis, but total levels of Ca^{2+} simply do not change much under transition metal-replete conditions. This would be consistent with the classification and biochemical characterization of the bacterial MgtA-like transporters as primarily Ca^{2+} transporters (48). In this model, only under conditions of acute Mn^{2+} toxicity does MgtA function as a Mn^{2+} transporter, a condition bolstered by increased accumulation of the MgtA in the membrane to effect efflux of this transition metal.

As a classic P_{II}-type ATPase, MgtA is predicted to transport two metal cations per reaction cycle, which could in theory involve any combination of Mn^{2+} or Ca^{2+} (48). This observation is not intuitive in terms of the basis of metal ion recognition by the transporter based on the significant chemical differences between Mn^{2+} and Ca^{2+}. However, it is not unprecedented. The dual metal specificity of MgtA offers striking functional parallels to the secretory pathway Ca^{2+}-ATPases (SPCAs) previously identified in yeast and vertebrates and known to transport both Mn^{2+} and Ca^{2+} into the Golgi from the cytosol. Here, the metal is used to metallate key client enzymes in this compartment or is simply secreted via this route (61–63). MgtA in fact shows significant sequence similarity to SPCAs and may well harbor the same Q747A substitution that enhances Mn^{2+} transport relative to Ca^{2+} (Supplementary Figure S12). Biochemical studies of *S. pneumoniae* MgtA coupled with more extensive physiological characterization of the functional role of MgtA are clearly required to further elucidate the metal-

dependence and functional role of the MgtA transport cycle.

SUPPLEMENTARY DATA

Supplementary Data are available at NAR Online.

ACKNOWLEDGEMENTS

We thank J.D. Helmann (Cornell University, NY) for providing the necessary plasmids and *B. subtilis* strains to make the *lacZ* reporter fusions and IPTG inducible constructs, H. Niu (Indiana University, IN) for providing all necessary reagents for the IVT assays, and the Y.X. Wang group (National Cancer Institute) for help collecting the SAXS data. We appreciate the support of the A.E. Simon's group (University of Maryland, College Park), and a special thanks to J. May for providing the necessary training for us to perform SHAPE profiling.

FUNDING

Idaho State University start up fund (to J.E.M.); Institutional Development Award from the National Institutes of General Medical Sciences [P20GM103408 to Idaho State University]; National Institutes of General Medical Sciences [R35 GM118157 to D.P.G., R01 GM042569-25S1 to J.E.M, R01 GM127715 to M.E.W.]. Funding for open access charge: Idaho State University start up funds (to J.E.M.).

Conflict of interest statement. The authors certify that they have no affiliations with or involvement in any organization or entity with any financial interests or non-financial interests in the materials discussed in this manuscript.

REFERENCES

1. Barrick,J.E., Corbino,K.A., Winkler,W.C., Nahvi,A., Mandal,M., Collins,J., Lee,M., Roth,A., Sudarsan,N., Jona,I. *et al.* (2004) New RNA motifs suggest an expanded scope for riboswitches in bacterial genetic control. *Proc. Natl. Acad. Sci. U.S.A.*, **101**, 6421–6426.
2. Meyer,M.M., Hammond,M.C., Salinas,Y., Roth,A., Sudarsan,N. and Breaker,R.R. (2011) Challenges of ligand identification for riboswitch candidates. *RNA Biol.*, **8**, 5–10.
3. Gottesman,S. (2004) The small RNA regulators of *Escherichia coli*: roles and mechanisms. *Annu. Rev. Microbiol.*, **58**, 303–328.
4. Storz,G., Vogel,J. and Wassarman,K.M. (2011) Regulation by small RNAs in bacteria: expanding frontiers. *Mol. Cell*, **43**, 880–891.
5. Waters,L.S. and Storz,G. (2009) Regulatory RNAs in bacteria. *Cell*, **136**, 615–628.
6. Wagner,E.G.H. and Romby,P. (2015) Small RNAs in bacteria and archaea: who they are, what they do, and how they do it. *Adv. Genet.*, **90**, 133–208.
7. Brantl,S. (2009) Bacterial chromosome-encoded small regulatory RNAs. *Future Microbiol.*, **4**, 85–103.
8. Repoila,F. and Darfeuille,F. (2009) Small regulatory non-coding RNAs in bacteria: physiology and mechanistic aspects. *Biol. Cell*, **101**, 117–131.
9. Majdalani,N., Vanderpool,C.K. and Gottesman,S. (2005) Bacterial small RNA regulators. *Crit. Rev. Biochem. Mol. Biol.*, **40**, 93–113.
10. Song,J., Lays,C., Vandenesch,F., Benito,Y., Bes,M., Chu,Y., Lina,G., Romby,P., Geissmann,T. and Boisset,S. (2012) The expression of small regulatory RNAs in clinical samples reflects the different life styles of *Staphylococcus aureus* in colonization vs. infection. *PLoS One*, **7**, e37294.
11. Xia,L., Xia,W., Li,S., Li,W., Liu,J., Ding,H., Li,J., Li,H., Chen,Y., Su,X. *et al.* (2012) Identification and expression of small non-coding RNA, L10-Leader, in different growth phases of *Streptococcus mutans*. *Nucleic Acid Ther.*, **22**, 177–186.
12. Ahmed,W., Zheng,K. and Liu,Z.F. (2016) Small non-coding RNAs: new insights in modulation of host immune response by intracellular bacterial pathogens. *Front. Immunol.*, **7**, 431.
13. Kröger,C., Dillon,S.C., Cameron,A.D., Papenfort,K., Sivasankaran,S.K., Hokamp,K., Chao,Y., Sittka,A., Hébrard,M., Händler,K. *et al.* (2012) The transcriptional landscape and small RNAs of *Salmonella enterica* serovar Typhimurium. *Proc. Natl. Acad. Sci. U.S.A.*, **109**, E1277–E1286.
14. Weiser,J.N., Ferreira,D.M. and Paton,J.C. (2018) *Streptococcus pneumoniae*: transmission, colonization and invasion. *Nat. Rev. Microbiol.*, **16**, 355–367.
15. O'Brien,K.L., Wolfson,L.J., Watt,J.P., Henkle,E., Deloria-Knoll,M., McCall,N., Lee,E., Mulholland,K., Levine,O.S., Cherian,T. *et al.* (2009) Burden of disease caused by *Streptococcus pneumoniae* in children younger than 5 years: global estimates. *Lancet.*, **374**, 893–902.
16. Collaborators, G.L.R.I. (2018) Estimates of the global, regional, and national morbidity, mortality, and aetiologies of lower respiratory infections in 195 countries, 1990–2016: a systematic analysis for the Global Burden of Disease Study 2016. *Lancet Infect. Dis.*, **18**, 1191–1210.
17. Chao,Y., Marks,L.R., Pettigrew,M.M. and Hakansson,A.P. (2014) *Streptococcus pneumoniae* biofilm formation and dispersion during colonization and disease. *Front. Cell Infect. Microbiol.*, **4**, 194.
18. Honsa,E.S., Johnson,M.D. and Rosch,J.W. (2013) The roles of transition metals in the physiology and pathogenesis of *Streptococcus pneumoniae*. *Front. Cell Infect. Microbiol.*, **3**, 92.
19. Becker,K.W. and Skaar,E.P. (2014) Metal limitation and toxicity at the interface between host and pathogen. *FEMS Microbiol. Rev.*, **38**, 1235–1249.
20. Livny,J., Brencic,A., Lory,S. and Waldor,M.K. (2006) Identification of 17 *Pseudomonas aeruginosa* sRNAs and prediction of sRNA-encoding genes in 10 diverse pathogens using the bioinformatic tool sRNAPredict2. *Nucleic Acids Res.*, **34**, 3484–3493.
21. Kumar,R., Shah,P., Swiatlo,E., Burgess,S.C., Lawrence,M.L. and Nanduri,B. (2010) Identification of novel non-coding small RNAs from *Streptococcus pneumoniae* TIGR4 using high-resolution genome tiling arrays. *BMC Genomics*, **11**, 350.
22. Tsui,H.C., Mukherjee,D., Ray,V.A., Sham,L.T., Feig,A.L. and Winkler,M.E. (2010) Identification and characterization of noncoding small RNAs in *Streptococcus pneumoniae* serotype 2 strain D39. *J. Bacteriol.*, **192**, 264–279.
23. Acebo,P., Martin-Galiano,A.J., Navarro,S., Zaballos,A. and Amblar,M. (2012) Identification of 88 regulatory small RNAs in the TIGR4 strain of the human pathogen *Streptococcus pneumoniae*. *RNA*, **18**, 530–546.
24. Sinha,D., Zimmer,K., Cameron,T.A., Rusch,D.B., Winkler,M.E. and De Lay,N.R. (2019) Redefining the sRNA transcriptome in*Streptococcus pneumoniae* Serotype 2 Strain D39. *J. Bacteriol.*, doi:10.1128/JB.00764-18.
25. Slager,J., Aprianto,R. and Veening,J.W. (2018) Deep genome annotation of the opportunistic human pathogen *Streptococcus pneumoniae* D39. *Nucleic Acids Res.*, **46**, 9971–9989.
26. Waters,L.S., Sandoval,M. and Storz,G. (2011) The *Escherichia coli* MntR miniregulon includes genes encoding a small protein and an efflux pump required for manganese homeostasis. *J. Bacteriol.*, **193**, 5887–5897.
27. Veyrier,F.J., Boneca,I.G., Cellier,M.F. and Taha,M.K. (2011) A novel metal transporter mediating manganese export (MntX) regulates the Mn to Fe intracellular ratio and *Neisseria meningitidis* virulence. *PLoS Pathog.*, **7**, e1002261.
28. Price,I.R., Gaballa,A., Ding,F., Helmann,J.D. and Ke,A. (2015) Mn(2+)-sensing mechanisms of *yybP-ykoY* orphan riboswitches. *Mol. Cell*, **57**, 1110–1123.
29. Dambach,M., Sandoval,M., Updegrove,T.B., Anantharaman,V., Aravind,L., Waters,L.S. and Storz,G. (2015) The ubiquitous *yybP-ykoY* riboswitch is a manganese-responsive regulatory element. *Mol. Cell*, **57**, 1099–1109.

30. Bachas,S.T. and Ferré-D'Amaré,A.R. (2018) Convergent use of heptacoordination for cation selectivity by RNA and protein metalloregulators. *Cell Chem. Biol.*, **25**, 962–973.
31. Rosch,J.W., Sublett,J., Gao,G., Wang,Y.D. and Tuomanen,E.I. (2008) Calcium efflux is essential for bacterial survival in the eukaryotic host. *Mol. Microbiol.*, **70**, 435–444.
32. Neef,J., Andisi,V.F., Kim,K.S., Kuipers,O.P. and Bijlsma,J.J. (2011) Deletion of a cation transporter promotes lysis in *Streptococcus pneumoniae*. *Infect. Immun.*, **79**, 2314–2323.
33. Rosch,J.W., Gao,G., Ridout,G., Wang,Y.D. and Tuomanen,E.I. (2009) Role of the manganese efflux system *mntE* for signalling and pathogenesis in *Streptococcus pneumoniae*. *Mol. Microbiol.*, **72**, 12–25.
34. Martin,J.E. and Giedroc,D.P. (2016) Functional determinants of metal ion transport and selectivity in paralogous cation diffusion facilitator transporters CzcD and MntE in *Streptococcus pneumoniae*. *J. Bacteriol.*, **198**, 1066–1076.
35. Lilley,D.J.M. (2000) Analysis of global conformation of branched RNA species using electrophoresis and fluorescence. *Methods Enzymol.*, **317**, 368–393.
36. Mortimer,S.A. and Weeks,K.M. (2007) A fast-acting reagent for accurate analysis of RNA secondary and tertiary structure by SHAPE chemistry. *J. Am. Chem. Soc.*, **129**, 4144–4145.
37. Wilkinson,K.A., Merino,E.J. and Weeks,K.M. (2006) Selective 2′-hydroxyl acylation analyzed by primer extension (SHAPE): quantitative RNA structure analysis at single nucleotide resolution. *Nat. Protoc.*, **1**, 1610–1616.
38. Rice,G.M., Busan,S., Karabiber,F., Favorov,O.V. and Weeks,K.M. (2014) SHAPE analysis of small RNAs and riboswitches. *Methods Enzymol.*, **549**, 165–187.
39. Karabiber,F., McGinnis,J.L., Favorov,O.V. and Weeks,K.M. (2013) QuShape: rapid, accurate, and best-practices quantification of nucleic acid probing information, resolved by capillary electrophoresis. *RNA*, **19**, 63–73.
40. Chen,B., Zuo,X., Wang,Y.X. and Dayie,T.K. (2012) Multiple conformations of SAM-II riboswitch detected with SAXS and NMR spectroscopy. *Nucleic Acids Res.*, **40**, 3117–3130.
41. Wang,Y.X., Zuo,X., Wang,J., Yu,P. and Butcher,S.E. (2010) Rapid global structure determination of large RNA and RNA complexes using NMR and small-angle X-ray scattering. *Methods*, **52**, 180–191.
42. Svergun,D.I. (1999) Restoring low resolution structure of biological macromolecules from solution scattering using simulated annealing. *Biophys. J.*, **76**, 2879–2886.
43. Blouin,S. and Lafontaine,D.A. (2007) A loop loop interaction and a K-turn motif located in the lysine aptamer domain are important for the riboswitch gene regulation control. *RNA*, **13**, 1256–1267.
44. Ren,A., Rajashankar,K.R. and Patel,D.J. (2012) Fluoride ion encapsulation by Mg2+ ions and phosphates in a fluoride riboswitch. *Nature*, **486**, 85–89.
45. Dann,C.E. 3rd, Wakeman,C.A., Sieling,C.L., Baker,S.C., Irnov,I. and Winkler,W.C. (2007) Structure and mechanism of a metal-sensing regulatory RNA. *Cell*, **130**, 878–892.
46. Wakeman,C.A., Ramesh,A. and Winkler,W.C. (2009) Multiple metal-binding cores are required for metalloregulation by M-box riboswitch RNAs. *J. Mol. Biol.*, **392**, 723–735.
47. Panja,S., Hua,B., Zegarra,D., Ha,T. and Woodson,S.A. (2017) Metals induce transient folding and activation of the twister ribozyme. *Nat. Chem. Biol.*, **13**, 1109–1114.
48. Dyla,M., Terry,D.S., Kjaergaard,M., Sorensen,T.L., Andersen,Lauwring, Andersen,J., J.P.,Rohde Knudsen, Altman,C., Nissen,R.B. and Blanchard,S.C. (2017) Dynamics of P-type ATPase transport revealed by single-molecule FRET. *Nature*, **551**, 346–351.
49. Sung,H.L. and Nesbitt,D.J. (2019) Single molecule FRET kinetics of the Mn(2+) riboswitch: evidence for allosteric Mg(2+) control of "induced fit" vs. "conformal selection" folding pathways. *J. Phys. Chem. B*, **123**, 2005–2015.
50. Martin,J.E., Lisher,J.P., Winkler,M.E. and Giedroc,D.P. (2017) Perturbation of manganese metabolism disrupts cell division in *Streptococcus pneumoniae*. *Mol. Microbiol.*, **104**, 334–348.
51. Huang,X., Shin,J.H., Pinochet-Barros,A., Su,T.T. and Helmann,J.D. (2017) *Bacillus subtilis* MntR coordinates the transcriptional regulation of manganese uptake and efflux systems. *Mol. Microbiol.*, **103**, 253–268.
52. Que,Q. and Helmann,J.D. (2000) Manganese homeostasis in *Bacillus subtilis* is regulated by MntR, a bifunctional regulator related to the diphtheria toxin repressor family of proteins. *Mol. Microbiol.*, **35**, 1454–1468.
53. Neef,J., Andisi,V.F., Kim,K.S., Kuipers,O.P. and Bijlsma,J.J. (2011) Deletion of a cation transporter promotes lysis in *Streptococcus pneumoniae*. *Infect. Immunity*, **79**, 2314–2323.
54. Osman,D., Foster,A.W., Chen,J., Svedaite,K., Steed,J.W., Lurie-Luke,E., Huggins,T.G. and Robinson,N.J. (2017) Fine control of metal concentrations is necessary for cells to discern zinc from cobalt. *Nat. Commun.*, **8**, 1884.
55. Osman,D., Martini,M.A., Foster,A.W., Chen,J., Scott,A.J.P., Morton,R.J., Steed,J.W., Lurie-Luke,E., Huggins,T.G., Lawrence,A.D. *et al.* (2019) Bacterial sensors define intracellular free energies for correct enzyme metalation. *Nat. Chem. Biol.*, **15**, 241–249.
56. Glasfeld,A., Guedon,E., Helmann,J.D. and Brennan,R.G. (2003) Structure of the manganese-bound manganese transport regulator of *Bacillus subtilis*. *Nat. Struct. Biol.*, **10**, 652–657.
57. Lisher,J.P., Higgins,K.A., Maroney,M.J. and Giedroc,D.P. (2013) Physical characterization of the manganese-sensing pneumococcal surface antigen repressor from *Streptococcus pneumoniae*. *Biochemistry*, **52**, 7689–7701.
58. Padilla-Benavides,T., George Thompson,A.M., McEvoy,M.M. and Arguello,J.M. (2014) Mechanism of ATPase-mediated Cu^{+} export and delivery to periplasmic chaperones: the interaction of *Escherichia* coli CopA and CusF. *J. Biol. Chem.*, **289**, 20492–20501.
59. Osman,D., Patterson,C.J., Bailey,K., Fisher,K., Robinson,N.J., Rigby,S.E. and Cavet,J.S. (2013) The copper supply pathway to a Salmonella Cu,Zn-superoxide dismutase (SodCII) involves P(1B)-type ATPase copper efflux and periplasmic CueP. *Mol. Microbiol.*, **87**, 466–477.
60. Utz,M., Andrei,A., Milanov,M., Trasnea,P.I., Marckmann,D., Daldal,F. and Koch,H.G. (2018) The Cu chaperone CopZ is required for Cu homeostasis in *Rhodobacter capsulatus* and influences cytochrome cbb3 oxidase assembly. *Mol. Microbiol.*, **111**, 764–783.
61. Durr,G., Strayle,J., Plemper,R., Elbs,S., Klee,S.K., Catty,P., Wolf,D.H. and Rudolph,H.K. (1998) The medial-Golgi ion pump Pmr1 supplies the yeast secretory pathway with Ca^{2+} and Mn^{2+} required for glycosylation, sorting, and endoplasmic reticulum-associated protein degradation. *Mol. Biol. Cell*, **9**, 1149–1162.
62. Vanoevelen,J., Dode,L., Van Baelen,K., Fairclough,R.J., Missiaen,L., Raeymaekers,L. and Wuytack,F. (2005) The secretory pathway Ca^{2+}/Mn^{2+}-ATPase 2 is a Golgi-localized pump with high affinity for Ca^{2+} ions. *J. Biol. Chem.*, **280**, 22800–22808.
63. Mukhopadhyay,S. and Linstedt,A.D. (2011) Identification of a gain-of-function mutation in a Golgi P-type ATPase that enhances Mn^{2+} efflux and protects against toxicity. *Proc. Natl. Acad. Sci. U.S.A.*, **108**, 858–863.